CHAPTER 2

Experiment

2.1 Materials

All chemicals used in the experiment are shown in Table 2.1.

Table 2.1 Chemicals, Molecular weight, Purity, and Company.

Chemical	Purity (%)	Molecular formula	Molecular Weight	Company
Ammonium metavanadate	99.50	NH_4VO_3	116.98	Ajax
Silver nitrate	99.80	$AgNO_3$	169.87	Sigma-Aldrich
Cobalt acetate tetrahydrate	98.00	$(CH_3COO)_2Co.4H_2O$	249.08	Sigma-Aldrich
Sodium hydroxide	97.00	NaOH	40.00	RCI Labscan
Titanium (IV) isopropoxide	97.00	$Ti[OCH(CH_3)_2]_4$	284.22	Sigma-Aldrich
Sodium metavanadate	98.00	$NaVO_3$	121.92	Sigma-Aldrich
Ethanol absolute	100.00	C_2H_5OH	46.08	Ajax
Ethylene glycol	99.00	$C_2H_6O_2$	62.07	QReC
Methylene Blue	100.00	$C_{16}H_{18}N_3SCl$	373.91	Fluka
Tert-butanol	99.92	$(CH_3)_3COH$	74.12	RCI Labscan
Ethylenediamine tetra acetic acid disodiumsalt (EDTA)	98.00	$[CH_2N(CH_2COOH)CH_2COONa]_2.2H_2O$	372.24	BDH

Table 2.1 Chemicals, Molecular weight, Purity, and Company (continued).

Chemical	Purity (%)	Molecular formula	Molecular Weight	Company
Propan-2-ol	99.80	$(CH_3)_2CHOH$	60.10	Labscan
p-Benzoquinone	98.00	$C_6H_4O_2$	108.09	Sigma-Aldrich
Terephthalic acid	97.00	$C_6H_4(COOH)_2$	166.13	BDH
Acetone	99.50	CH_3COCH_3	58.08	RCI Labscan
Methanol	99.80	CH_3OH	32.04	QreC
Potassium bromide	99.00	KBr	119.00	Sigma-Aldrich
Triethanolamine	75.00	$C_6H_{15}NO_3$		M & B

2.2 Instruments

1. UV–vis diffuse reflectance spectrophotometer (UV–vis DRS), Lambda 950
2. UV–vis spectrophotometer, Shimazu 1600 and Shimadzu UV3600 with integrating sphere assembly
3. X-ray diffractometer (XRD)-Rigaku MiniFlex II, GBC EMMA 0133
4. Scanning electron microscope (SEM) and energy dispersive X-ray spectroscope (EDS), JEOL JSM6335F, SEM-JOEL JSM 5910LV
5. Brunauer–Emmett–Teller (BET)–Micromeritics Tristar 3000, Quantachrome NOVA 1000
6. X-ray photoelectron spectroscope (XPS), Perkin Elmer 5100/ESCA Al Kα
7. Fourier transforms infrared spectrophotometer (FTIR), Nicolet, IR510
8. Halogen lamp, Phillips, 50 W (intensity of ~640 W/m^2)
9. Magnetic stirrer and magnetic bar
10. Black box
11. pH meter, TPS 900P-EUTECH PC 5500
12. Quartz cell
13. Porcelain Crucible with Lid: High Form, 40 mm Diameter x 25 mm Capacity
14. Centrifuge, Universal 320, Eppendorf 5702
15. Centrifuge tube

16. Hot plate and stirrer, IKA C-MAG HS7
17. Oven, Memmert 70
19. Photoluminescence, AvaSpec-2048TECUSB2-2 spectrophotometer
20. Muffle furnace, CWF1200 - Carbolite
21. Acid Digestion Vessels, Polytetrafluoroethylene (PTFE) liner – Parr Instrument Company
22. Oven, ED FD model ED 53 - Binder
23. Ultrasonic cleaner
24. Plastic cuvette, Poly(methyl methacrylate), PMMA 2.5 mL, 12.5 x 45 mm. – GMBH brand
25. Micropipette, Biopette auto clavable – Labnet 100-1000 µL

2.3 Sample Preparation

2.3.1 Preparation of silver vanadate (Ag_3VO_4)

Pure Ag_3VO_4 was prepared via hydrothermal method with silver nitrate ($AgNO_3$) and sodium metavanadate ($NaVO_3$) as precursors. $AgNO_3$ 3 mmol and 1 mmol of $NaVO_3$ were separately dissolved in 10 mL and 70 mL of deionized water (DI-water) respectively. The homogenous $AgNO_3$ solution was poured slowly into $NaVO_3$ solution, and the yellow precipitate instantly appeared. The pH of precipitate solution was adjusted to 11 by sodium hydroxide (NaOH) which is the appropriate pH solution for synthesized pure phase of Ag_3VO_4 via hydrothermal method. This yellow precipitate solution was kept overnight in refrigerator at about 20.0 °C. The 75.00 mL suspension was transferred into Teflon liner 125 mL heating at 140 °C for 8 h. The solution in Teflon liner was poured out, and the precipitate of Ag_3VO_4 was washed with DI-water several times until the supernatant was neutralized. The precipitate was heated in oven at 70 °C for 4 h.

2.3.2 Preparation of cobalt titanate ($CoTiO_3$)

$CoTiO_3$ particle was synthesized by sol-gel method using cobalt acetate tetrahydrate $(CH_3COO)_2Co.4H_2O$, titanium (IV) isopropoxide (TTIP), and ethylene glycol as complexing agent. The 0.015 mol of cobalt acetate was dissolved in 100 mL of ethylene glycol, after 10 min the light pink solution was formed. The 0.01 mol of TTIP was added into the previous solution, and aged at room temperature for 22 h to finally obtain cloudy pink sol. The cloudy pink sol was collected by ultracentrifuge, and heated at 70

°C for 22 h. The gel-liked appeared. Then, the cloudy pink gel was calcined at 800 °C for 4 h to form pure light green $CoTiO_3$ powder.

2.3.3 Preparation composite materials between Ag_3VO_4 and $CoTiO_3$ ($Ag_3VO_4/CoTiO_3$)

The preparation of $Ag_3VO_4/CoTiO_3$ composite materials in various ratios was similar to that of Ag_3VO_4, except that a certain amount of preformed $CoTiO_3$ was firstly dispersed in $NaVO_3$ solution. The $AgNO_3$ solution was then poured into the mixture to obtain $Ag_3VO_4/CoTiO_3$ composite. The various ratios of $Ag_3VO_4/CoTiO_3$ composite are prepared which are 10 wt%, 30 wt%, 50 wt%, 70 wt%, 90 wt% of chemical mixture, and 50 wt% of physical mixture.

2.4 Sample characterizations

2.4.1 X-ray diffraction (XRD) [1-2]

The identified phase can be compared with Joint Committee on Powder Diffraction Standards (JCPDS) files which contain diffraction peak data. The different atomic position in each compounds leads to different positions of peak signal in XRD pattern. The diffraction pattern can be described by Bragg's law to identify the phase of the sample corresponding to the Eq. 2.1.

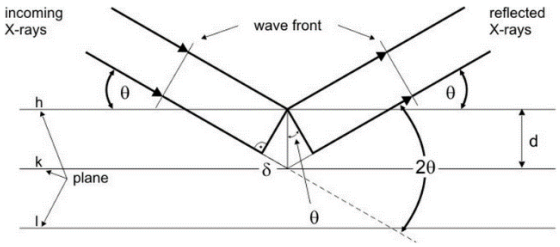

Fig. 2.1 Bragg's law reflections [3].

$$n\lambda = 2d_{hkl} \sin\theta_{hkl} \quad (2.1)$$

where d_{hkl} is the d-spacing, interplanar distance between (*hkl*) planes, θ is the incident angle, n is the order of diffraction, and λ is the wavelength of incident X-ray (1.541 Å). Interplanar distance and (*hkl*) lattice planes can either be found from JCPDS file or calculated by using the following equations. Eq. 2.2 and 2.3 is used for calculation of

lattice parameters of $CoTiO_3$ hexagonal structure and Ag_3VO_4 monoclinic system, respectively.

For hexagonal crystal system;
$$\frac{1}{d^2} = \frac{4}{3}\left[\frac{h^2 + hk + k^2}{a^2}\right] + \frac{l^2}{c^2} \quad (2.2)$$

For monoclinic crystal system;
$$\frac{1}{d^2} = \frac{1}{\sin^2\beta}\left[\frac{h^2}{a^2} + \frac{k^2\sin^2\beta}{b^2} + \frac{l^2}{c^2} - \frac{2hl\cos\beta}{ac}\right] \quad (2.3)$$

where, d_{hkl} is the d-spacing; a, b, c are sides of the unit cell; and *h*, *k*, *l* are the Miller indices.

The intensity of XRD pattern can be related to crystallinity of crystal sample. In addition, crystallite size can be calculated by Scherrer's equation (Eq. 2.4).

$$L = \frac{K\lambda}{\beta\cos\theta} \quad (2.4)$$

where L = Crystallite size

λ = Wavelength of X-ray radiation (Cu Kα = 0.1541 nm)

K = Scherrer shape factor (taken as 0.89)

β = Line width at half maximum height (FWHM)

θ = Diffraction angle at maximum intensity

Crystal structures of the samples are examined by XRD using the Rigaku MiniFlex II with CuK_α radiation (λ = 0.1541 nm) at a scanning speed of 8°/min. The analysis is typically conducted within the 2θ range of 15−80°.

2.4.2 Scanning electron microscope (SEM) [4-6]

To investigate the microstructure morphology and chemical composition, characterization of sample, SEM is chosen for analysis. Owing to unaided eye discrimination (resolution) of human is only about 0.1 mm, so magnification of SEM can provide high resolution image in the range of micrometer to nanometer to easily observe microstructure of sample. SEM is proved that the limit of resolution depends on the wavelength of the illumination source. Source of SEM is electron gun which can produce electron to interact with the sample. The interaction between electron and surface of the sample produces two main signal forms which are secondary electron and

backscattering electron (BSE). Secondary electron results from primary electron beam colliding with atom in the sample, and lose substantial energy to emit loosely bound electron in the form of secondary electron. In the part of backscattering electron which has higher penetrating energy, carry information in deep level as comparing to secondary electron. The BSE results from the primary electron beam interacting with the nucleus of the sample, and bounces off in the wide angle depending on the atomic weight component in the sample. Therefore, BSE image provides more contrast image than secondary electron image. The processes of electron-sample interactions are shown in Fig. 2.2.

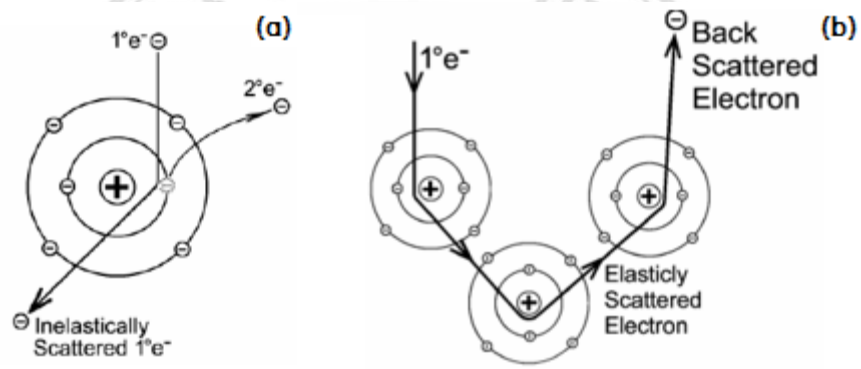

Fig. 2.2 The process of electron interaction with the electron in atomic sample to produce secondary electron (a) and back scattering electron (b) signal respectively [5].

In this research, we will use only the signal from secondary electron to describe the surface morphology of synthesized particle. The schematic of SEM is shown in Fig. 2.3.

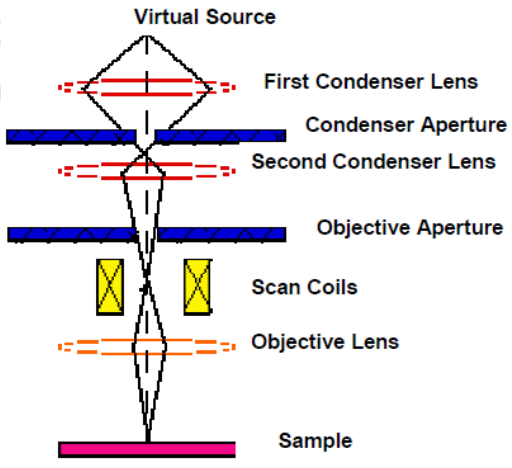

Fig. 2.3 The schematic of SEM technique [7].

Others illuminated signal can be produced by interaction between primary electron beam and the sample such as characteristic X-ray, and auger electron which are shown in Fig.2.4. Moreover, the characteristic X-ray illumination is used in energy dispersive X-ray spectrophotometry (EDS) technique to quantify the elemental component in the sample.

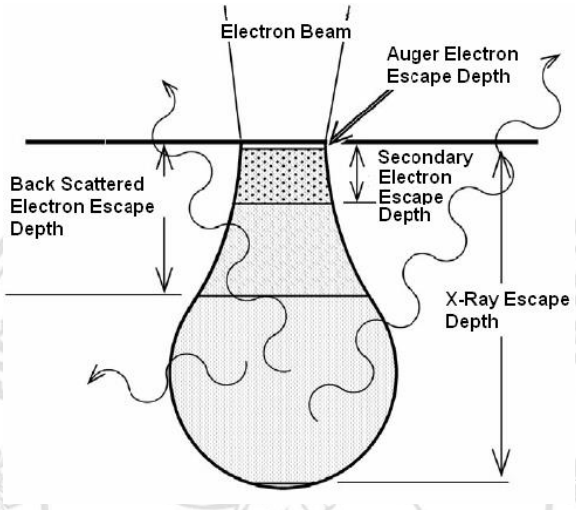

Fig. 2.4 The path length of electron penetration can produce different signals for use in various techniques [8].

2.4.3 Ultraviolet-visible spectroscopy (UV-vis spectroscopy) [9-15]

In this study UV-vis spectroscopy is used to verify a decrease of organic pollutant (methylene blue) as a function of irradiation time. In order to observe the degradation rate of methylene blue the sample was taken at 30 min time interval to measure light absorption which proportionally corresponds to the concentration of methylene blue according to Beer Lambert's law relationship.

The ratio I / I_o is known as transmittance T and the logarithm of the inverse ratio I_o / I is known as the absorbance A (Eq. 2.5-2.7)

$$-Log\frac{I}{I_0} = -\log T = \varepsilon cl \tag{2.5}$$

$$Log\frac{I_0}{I} = A = \varepsilon cl \tag{2.6}$$

$$A = \varepsilon cl \tag{2.7}$$

where I_o = Intensity of the incident light (or the light intensity passing through a reference cell)

I = Intensity of light transmitted through the sample solution

c = concentration of the solute (mol l^{-1})

l = path length of the sample (cm)

ε = molar absorptivity which is a characteristic constant of an absorbing species in a particular solvent, and wavelength calculated at concentration equal to 1 mol l^{-1} with path length equal to 1 cm^{-1} ($l.mol^{-1} cm^{-1}$).

UV-vis diffuse reflectance spectroscopy, (UV-vis DRS) is an important technique for the measurement of band gap energy of semiconductor photocatalyst. Normally, the UV-vis absorption spectroscopy is used to characterize semiconductors thin films. Due to low scattering in solid films, it is possible to extract the E_g values from their absorption spectra knowing their thickness. However, in colloidal samples, the scattering effect is enhanced since more superficial area is exposed to the light beam. On the other hand, it is common to obtain powdered samples instead of thin films or colloids, and frequently UV-vis absorption spectroscopy is carried out by dispersing the sample in liquid media such as water, ethanol or methanol. If the particle size of the sample is not small enough, it precipitates and the absorption spectrum is even more difficult to interpret. In order to avoid these complications, it is desirable to use DRS, which provides more reliable E_g of materials.

The sample for UV-vis DRS characterization is flattening or pressing into a pellet to form the oriented crystal. In specular reflectance, the light reflected from a sample has an angle of reflectance equal to the angle of an incident light. The main component of UV-vis DRS instrument is an integrating sphere. This integrating sphere consists of a spherical chamber (50-300 mm diameter) which inner wall made of barium oxide coating, a material that provides the maximum reflectance over the entire visible wavelength range. The light is multiply reflected at the surface of the sphere and eventually reaches the optical detector for detection and measurement. The obtained value is the relative reflectance with respect to the reflectance of the reference standard white board, which is taken to be 100%.

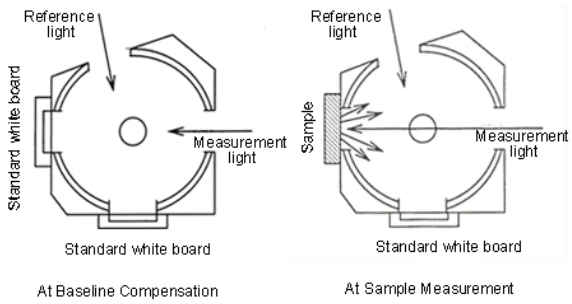

Fig. 2.5 Schematic of band gap measurement by UV-vis DRS technique [16].

Kubelka and Munk proposed the Kubelka-Munk function to describe behavior of light travelling inside a light scattering specimen, which is based on the following differential equation (Eq. 2.8-2.9).

$$idi = i(S+K)idx + Sjdx \tag{2.8}$$

$$dj = i(S+K)jdx + Sidx \tag{2.9}$$

where i and j are the intensities of light traveling inside the sample towards its unilluminated and illuminated surfaces, respectively

dx is the differential segment along the light path

S and K are the K-M scattering and absorption coefficients, respectively

In the limiting case of an infinitely thick sample, thickness and sample holder have no influence on the value of reflectance (R). In this case, the Kubelka-Munk equation at any wavelength becomes (Eq. 2.10):

$$\frac{K}{S} = \frac{(1-R_\infty)^2}{2R_\infty} \equiv F(R_\infty) \tag{2.10}$$

where $F(R_\infty)$ = the so-called remission function or Kubelka-Munk function (Eq. 2.11),

$$R_\infty = R_{sample}/R_{standard} \tag{2.11}$$

In the parabolic band structure, E_g, and absorption coefficient α of a direct band gap semiconductor are related through Eq. 2.12.

$$\alpha h\nu = C_1(h\nu - E_g)^{1/2} \tag{2.12}$$

where α is the linear absorption coefficient of the material,

$h\nu$ is the photon energy

C_1 is a proportionality constant.

When the material scatters in perfectly diffuse manner (or when it is illuminated at 60± incidence), the K-M absorption coefficient K becomes equal to 2α (K=2α). In this case, considering the K-M scattering coefficient S as constant with respect to wavelength, and using the remission function the expression in Eq. 2.13 can be obtained.

$$[F(R_\infty)hv]^2 = C_2(hv - E_g) \quad (2.13)$$

where R_∞ is the diffuse reflectance of the examined samples ($R_\infty = R_{Sample}/R_{Standard}$)

$F(R_\infty)$ is remission or Kubelka-Munk function

E_g is optical band gap energy

C_2 is a proportionallity constant.

The white barium sulphate powder, $BaSO_4$ is used as a reference standard due to its complete reflection of incident light properties in UV-vis range. Plotting the $[F(R_\infty)\ hv]^2$ against hv, the band gap E_g of a powder sample can be extracted.

2.4.4 Photocatalytic activity test

The degradation of organic pollutant was studied via black box photocatalytic activity test. Methylene blue, as one of widely used organic dye in the industrial factories, composes of aromatic ring and conjugate diene and is difficult to decompose. Therefore, in this research we are interested in studying the degraded methylene blue by semiconductor heterogeneous catalyst. In the first step, catalyst was dispersed in the dye solution by sonication for 15 minutes. Under magnetic stirring, the adsorption between dye solution and heterogeneous catalyst was kept in the dark for 1 hour, followed by light irradiation for 3 h. The light source anchored on the top of black box is 50 W halogen lamp providing mostly visible light irradiation. At 30 min interval, 5 ml of the sample was taken out and the heterogeneous catalyst was separated by ultracentrifugation. The solution was measured with UV-vis spectroscopy technique to evaluate the decrease in concentration of methylene blue as the function of irradiated time. The characteristic maximum wavelength of methylene blue can be observed about 664 nm.

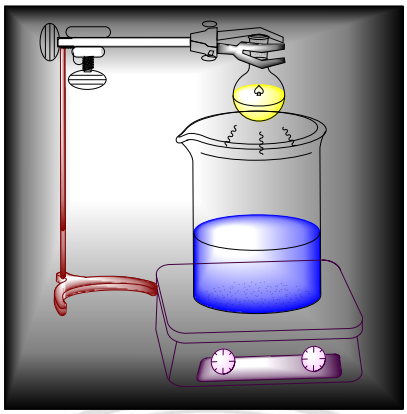

Fig. 2.6 Photocatalytic set up in the black box.

2.4.5 Photoluminescence (PL) [17-19]

Photoluminescence spectrophotometer was used in this research to describe the electronic properties of heterojunction semiconductor photocatalyst. Depending on the electronic arrangement, the various combination of electron spin and orbital angular momenta results in different atomic energy states. The term symbols are used to represent the angular momenta of these individual atomic states. The total electron spin quantum number is represented by *S*. The total electron spin quantum number can be used to calculate the spin multiplicity (2S+1) which is the number of possible values of electron spin momentum. If all electrons pair (S = 0), there is only one arrangement (2S+1=1) and the state is called a singlet state. If there is one unpaired electron (S = 1/2), there are two arrangement (2S+1=2) and the state is doublet. If there are two unpaired electrons (S = 1), there are three arrangement (2S+1=3) and the state is a triplet. A schematic energy-level diagram is shown in Fig. 2.7.

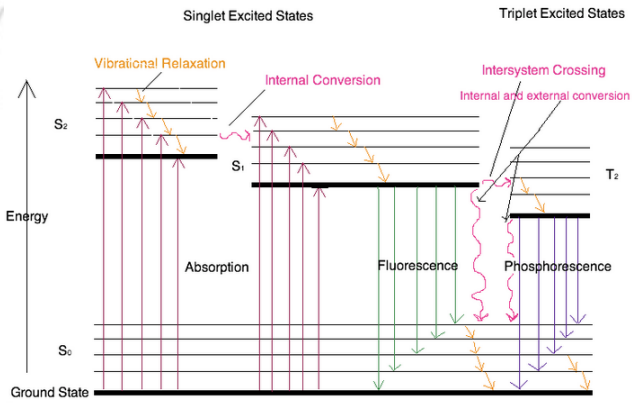

Fig. 2.7 Partial Jablonski Diagram for Absorption, Fluorescence, and Phosphorescence [20].

The absorption of appropriate radiant energy by a molecule raises the molecule from a vibrational level in the ground state to one of many vibrational levels in one of excited electronic levels, usually the first excited singlet state, S_1. The absorption step occurs within 10^{-15} s. A number of vibrational states are populated immediately following absorption. However, molecules in a higher vibrational level of the excited singlet state quickly return to the lowest vibrational level of the excited state by transferring their excess energy to other molecules through collisions. Fluorescence results from the spontaneous radiative transition that occurs when molecules return to the ground electronic state level. This radiative process has a short lifetime (about 10^{-8} s) so that in many molecules it can compete effectively with other processes capable of removing the excitation energy, such as internal conversion or intersystem crossing. If the potential energy curve of the singlet state crosses that of the triplet state, some singlet state molecules may pass over to the lowest triplet state via an intersystem crossing which involves vibrational coupling between the excited singlet state, S_1, and the triplet state, T_1. Although singlet-triplet transitions are forbidden process, there is some probable transition of excited singlet state to the triplet state because the energy of the lowest vibrational level of the triplet state is lower than that of the singlet state. The vibrational energy will be lost by radiationless transitions to the vicinity of the zero point vibrational level of the triplet state. The molecule then will return to a vibrational level of the ground state and constitute to phosphorescence emission. Consequently, the triplet state persists for a relatively long average lifetime and the rate of phosphorescence emission is very slow (10^{-2} to 100 s). Spin-orbit coupling, which is a magnetic perturbation capable of flipping spins is believed to be the main source of phosphorescence transition back to the ground singlet state. While some deactivation of excited state molecules may occur as a result of collisions with solvent molecules before the energy is reemitted as fluorescence, this effect becomes predominant in phosphorescence due to its long lifetime transition. Phosphorescence is virtually unknown for dissolved molecules and can only be observed when the phosphor is frozen into glasses at low temperatures so that collisional deactivation is prevented or at least severely restricted.

In both fluorescence and phosphorescence the lower energy photon is emitted in an arbitrary direction and at longer wavelength than the excited wavelength. The instrumentation is shown in Fig. 2.8.

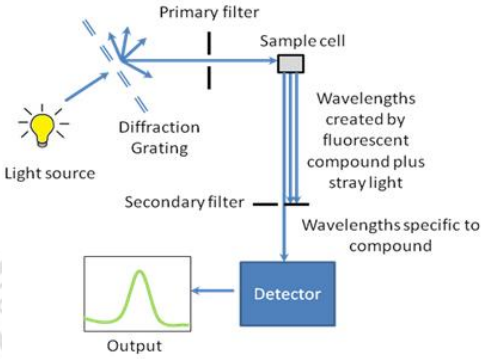

Fig. 2.8 Schematic of PL characterization [21].

In this research, the laser source of PL activates electrons in the valence band of semiconductor to the conduction band or ground state to excited state. These activated electrons emit the excess energy in the form of luminescence.

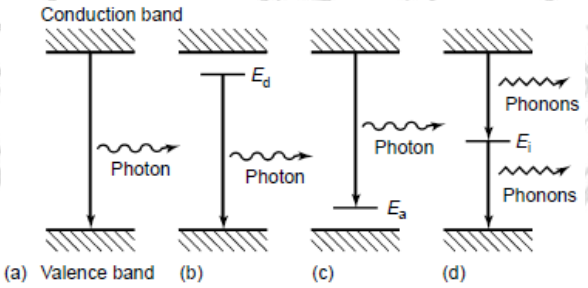

Fig. 2.9 (a–c) Radiative recombination paths: (a) band-to band; (b) donor to valence band; (c) conduction band to acceptor. (d) non-radiative recombination via an intermediate state [19].

In the bulk of a crystalline material, translational symmetry leads to the formation of electronic energy bands. Fig. 2.9 shows that defects and impurities break the periodicity of the lattice and perturb the band structure locally. The perturbation usually can be characterized by a discrete energy level that lies within the band gap. Depending on the defect or impurity, the state acts as a donor or acceptor of excess electrons in the crystal. Electrons or holes are attracted to the excess or deficiency of local charge due to the impurity nucleus or defect, and Coulomb interaction occurs. The energy of the emitted light can be analyzed to determine the energy of the defect or impurity level. Shallow

levels, which lie near the conduction or valence band edge, are more likely to participate in radiative recombination.

2.4.6 Fourier-transform Infrared Spectroscopy (FTIR) [22-23]

Infrared spectroscopy is a technique based on the vibrations of the atoms of a molecule. An infrared spectrum is commonly obtained by passing infrared radiation, the one region of the electromagnetic wave involving those of vibration and rotation processes which can be represented in terms of quantized discrete energy levels, through a sample and determining the fraction of the incident radiation which is absorbed at a particular energy. The energy at which any peak in an absorption spectrum appears corresponds to the frequency of a vibration of a part of a sample molecule.

For a molecule to show infrared absorptions it must possess a specific feature. An electric dipole moment of the molecule must change during the vibration. This is the selection rule for infrared spectroscopy. Fig. 2.10 illustrates an example of an 'infrared-active' molecule, a heteronuclear diatomic molecule. The dipole moment of such a molecule changes as the bond expands and contracts. By comparison, an example of an 'infrared-inactive' molecule is a homonuclear diatomic molecule because its dipole moment remains zero no matter how long the bond is.

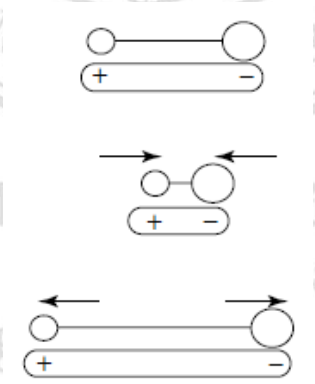

Fig. 2.10 Changes in the dipole moment of a heteronuclear diatomic molecule [22].

The interactions of infrared radiation with matter can be understood in terms of changes in molecular dipoles associated with vibrations and rotations. In order to begin with a basic model, a molecule can be looked upon as a system of masses joined by bonds with spring-like properties. For a diatomic molecule, only one vibration that corresponds to

the stretching and compression of the bond is possible. This accounts for one degree of vibrational freedom.

Polyatomic molecules containing many (*N*) atoms will have 3*N* degrees of freedom. Looking first at the case of molecules containing three atoms, two groups of triatomic molecules may be distinguished, i.e. linear and non-linear. Two simple examples of linear and non-linear triatomics are represented by CO_2 and H_2O, respectively (Fig. 2.11). Both CO_2 and H_2O have three degrees of translational freedom. Water has three degrees of rotational freedom, but the linear molecule carbon dioxide has only two since no detectable energy is involved in rotation around the O=C=O axis. Subtracting these from 3*N*, there are 3*N*−5 degrees of freedom for CO_2 (or any linear molecule) and 3*N*−6 for water (or any non-linear molecule). *N* in both examples is three, and so CO_2 has four vibrational modes and water has three. The degrees of freedom for polyatomic molecules are summarized in Table 2.2. In addition, vibrations can involve either a change in bond length (stretching) or bond angle (bending). Some bonds can stretch in-phase (symmetrical stretching) or out-of-phase (asymmetric stretching).

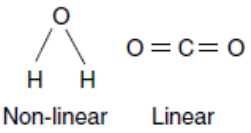

Fig. 2.11 Carbon dioxide and water molecules [22].

Table 2.2 Degrees of freedom for polyatomic molecules. From Stuart, B., Modern Infrared Spectroscopy, ACOL Series, Wiley, Chichester, UK, 1996. University of Greenwich, and reproduced by permission of the University of Greenwich.

Type of degrees of freedom	**Linear molecules**	**Non-linear molecules**
Translational	3	3
Rotational	2	3
Vibrational	3*N*-5	3*N*-6
Total	3*N*	3*N*

Two other concepts are also used to explain the frequency of vibrational modes. These are the stiffness of the bond and the masses of the atoms at each end of the bond. The stiffness of the bond can be characterized by a proportionality constant termed as force constant, k (derived from Hooke's law). The reduced mass, μ, provides a useful way of

simplifying our calculations by combining the individual atomic masses which can be expressed as follows (Eq. 2.14).

$$\mu = \frac{m_1 m_2}{(m_1 + m_2)} \tag{2.14}$$

where m_1 and m_2 are the masses of the atoms at the ends of the bond.

The equation relating the force constant, the reduced mass and the frequency of absorption is shown in Eq. 2.15.

$$\bar{\nu} = \frac{1}{2\prod c}\sqrt{\frac{k}{\mu}} \tag{2.15}$$

where c is the speed of light

$\bar{\nu}$ is the wavenumber for bond vibrational frequencies

One of the great advantages of infrared spectroscopy is that virtually any sample in any state may be studied. Liquids, solutions, pastes, powders, films, fibres, gases and surfaces can all be examined with a judicious choice of sampling technique.

2.4.7 Brunauer Emmett Teller method (BET) [24-28]

Information on surface characteristics is very important for the possible applications of semiconductors and heterogeneous catalysts. Surface area is used by catalyst manufacturers and users to monitor the activity and stability of a catalyst. The three isotherm equations which are most frequently used are Langmuir, Freundlich and Brunauer Emmett Teller (BET). The theory of Brunauer Emmett Teller is an extension of Langmuir treatment which allows for multilayer adsorption on non-porous solid surfaces. The BET equation is derived by balancing the rates of evaporation and condensation for the various adsorbed molecular layers, and is based on the simplifying assumption that a characteristic heat of adsorption ΔH_1 applies to the first monolayer, while the heat of liquefaction, ΔH_L, of the vapour in question applies to adsorption in the second and subsequent molecular layers. The equation is usually written in Eq. 2.16.

$$\frac{p}{V(p_0 - p)} = \frac{1}{V_m c} + \frac{(c-1)}{V_m c}\frac{p}{p_0} \tag{2.16}$$

where p_0 is the saturation vapour pressure

V_m is the monolayer capacity

c is constant ≈ exp [$(\Delta H_L - \Delta H_1)/RT$]

The BET model can also be applied to a situation which might be applicable to porous solids. If adsorption is limited to n molecular layers (where n is related to the pore size), the equation is obtained as shown in Eq. 2.17.

$$V = \frac{V_m cx}{(1-x)} \cdot \frac{1-(n+1)x^n + nx^{n+1}}{1+(c-1)x - cx^{n+1}} \tag{2.17}$$

where $x = \frac{p}{p_0}$

This equation is a general expression which reduces to the Langmuir equation when n=1 and to the BET equation when n = ∞

Usually, the solid adsorbent under investigation must first be freed, as far as possible from previously adsorbed gases and vapours. Evacuation to 10^{-4} Torr (outgassing) for several hours will usually remove physically adsorbed gas. To remove gas completely, the solid is heated to a high temperature (100-400 °C).

To determine the surface area, the monolayer capacity, V_m, is a parameter of particular interest since it can be used for calculating the surface area of an adsorbent. If the BET equation is applicable to a multilayer physical adsorption isotherm, a plot of $\frac{p}{V(p_0 - p)}$ versus $\frac{p}{p_0}$ gives a straight line of slope $\frac{(c-1)}{V_m c}$ and the intercept of $\frac{1}{V_m c}$ on the $\frac{p}{V(p_0 - p)}$ axis.

$$V_m = \frac{1}{slope + \text{int}\ ercept} \tag{2.18}$$

The straight line pass through the origin, and V_m can be calculated on the basis of a single gas adsorption measurement. The adsorbate most commonly used for BET surface area determination is nitrogen gas at 77 K (liquid nitrogen temperature) because the value of c is generally high enough to give a well-defined point B (Fig. 2.12), but

not too high to give excessive localization of adsorption. The effective area occupied by each adsorbed nitrogen molecule at monolayer capacity can be calculated from the density of liquid nitrogen (0.81 g/cm^{-3}) on the basis of closed pack spheres model. Therefore, the cross section area is 16.2 x 10^{-20} m^2.

Moreover, Brunauer has mainly classified adsorption isotherms into the five characteristic types shown in Fig. 2.12. To facilitate comparison of adsorption isotherms, it is preferable to plot them in terms of relative pressure (p/p_0), where p_0 is the saturation vapor pressure. This also has the advantage of giving a 0 to 1 scale for all gases.

Type I isotherm (e.g. ammonia on charcoal at 273 K) shows a fairly rapid rise in the amount of adsorption with increasing pressure up to a limiting value. It is referred to as Langmuir-type isotherm and is obtained when adsorption is restricted to a monolayer. Chemisorption isotherm, therefore, approximates to this shape. Type I isotherms have also been found for physical adsorption on solids containing a very fine pore structure.

Type II isotherm (e.g. nitrogen on silica gel at 77 K) is frequently encountered, and represents- multilayer physical adsorption on non-porous solids. It is often referred to sigmoid isotherm. For such solids, point B represents the formation of an adsorbed monolayer. Physical adsorption on microporous solids can also result in type II isotherm. In this case, point B represents both monolayer adsorption on the surface as a whole and condensation in the fine pores. The remainder of the curve represents multilayer adsorption as non-porous solids.

Type III isotherm (e.g. benzene on iron (III) oxide gel at 320 K) levels off near the saturation vapour pressure and is considered to reflect capillary condensation in porous solids, the effective pore diameters usually are between 2 nm and 20 nm. The upper limit of adsorption is mainly governed by the total pore volume.

Type IV isotherm (e.g. bromine on silica gel at 352 K) and type V isotherms (e.g. water vapour on charcoal at 373 K) show no rapid initial uptake of gas which usually occur when the forces of adsorption in the first monolayer are relatively small. These isotherms are rare.

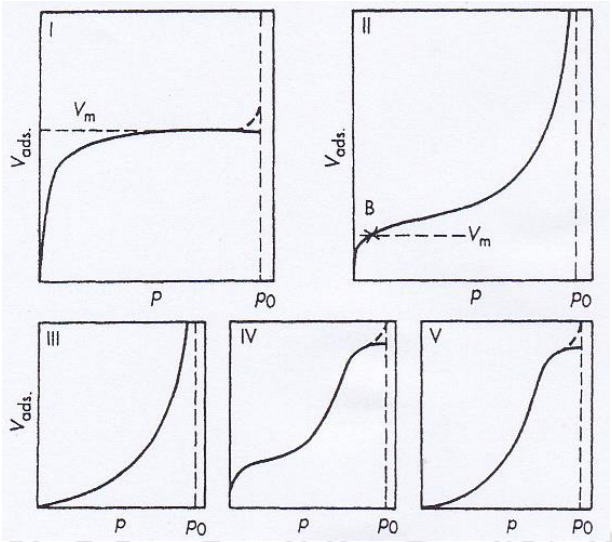

Fig. 2.12 Brunauer's classification of adsorption isotherm (p_0 is saturated vapour pressure) [24].

2.4.8 X-ray fluorescence Analysis (XRF) [29-30]

Conventional X-ray fluorescence analysis is known by several other names, such as X-ray emission spectrometry, X-ray fluorescence spectrometry, wavelength dispersive X-ray fluorescence spectrometry, and so on.

X-ray fluorescence analysis is a rapid, non-destructive, qualitative, and quantitative method of determining element in solids and liquids. XRF based on the measurement of wavelengths and intensities of X-rays emitted by a sample, when excited by the rays from a primary X-ray tube. It is essentially a surface technique since the primary beam penetrates for a few micrometers in heavy element such as gold, and about half a millimeter for the lighter element such as aluminium. The X-ray wavelength is less than the K, L, and M absorption edges of atoms in the sample which have enough sufficient energy to remove K, L, or M electrons from the sample atoms. Subsequent movement of electrons from outer levels into these vacant positions give rise to the emission of characteristic radiation X-rays of definite wavelengths. These wavelengths are separated by reflection on the crystal when the Bragg's equation is fulfilled. Fig. 2.13 shows the layout of a typical X-ray spectrometer.

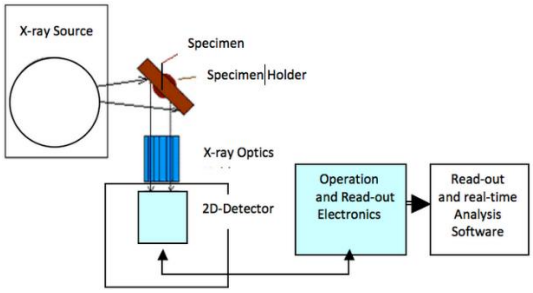

Fig. 2.13 Lay out of XRF [31].

A primary X-ray beam irradiates the sample (A) causing it to fluoresce. Each element emitting its own characteristic X-ray radiation. Part of the radiation is collimated by a system of slits (B) onto an analyzing crystal (C). The crystal is mounted on a turnable holder which can be rotated by a motor. As the crystal rotates, so the angle θ presented to the fluorescent rays changes. The Bragg's equation is fulfilled for a particular X-ray wavelength when $\sin\theta = n\lambda/2d$, this part of the beam is reflected by the crystal. The reflected beam passes through a set of collimating slits (D) and enters the detector (E). When the crystal rotates through an angle, θ the detector rotates through 2θ. Therefore, the detector is always being in the correct position to receive reflected rays by the crystal.

For qualitative analysis, the crystal is rotated. The X-ray and crystal angle is rotated between 15°and 145°, a scale of 2θ is automatically recorded. The elements are identified from their 2θ values in conjunction with an appropriate set of tables.

For quantitative analysis, the crystal remains stationary, set at the appropriate angle to reflect a particular elemental concentration in the sample. The stationary mode is also used to determine thin films, which intensity is proportional to the thickness depending on the operating conditions of the X-ray tube. XRF can identify the concentration ranging from fractional part per million (ppm) to 100%, and can detect element from Be to U in the periodic table.

For quantitative work, bulk solids should ideally be in the form of a thin cylinder about 5 cm in diameter with smooth surface to eliminate surface texture effect. To ensure homogeneity and to eliminate particle size effect, the powder is usually milled to about 300 mesh. They may be loosely compacted into a pellet.

2.4.9 Energy Dispersive X-ray analysis (EDX) [29]

Energy dispersive X-ray separates characteristic X-ray on the basis of their photon energies used as an accessary to other instruments such as the electron microscope. Characteristic X-ray from a specimen irradiated with a primary X-ray beam enters a cooled Si(Li) detector which is connected to an amplifier system. It is necessary to cool the detector in liquid nitrogen temperature in order to reduce electronic noise, and to ensure optimum resolution. The detector acts as a transducer converting X-ray photons to charge. The charge produced is directly proportional to the energy of the X-rays detected. To be more precise, the detector converts the X-ray photons into electron-hole pairs, which are then swept out of the detector by an applied voltage. The signal enters the analogue-to-digital convertor (ADC). Each time a pulse is produced by the ADC, a number is generated that represents a channel to be incremented by one, each channel representing a small range of energy. The data go to a multi-channel analyser which accumulates the energy spectrum. A spectrometer having a 1000-channel analyser covering the photon-energy range 0-20 keV, would typically have 20 eV per channel. The data are accumulated until one channel has accumulated a preset number of counts. The spectrum is displayed as a series of peaks on an X-Y plotter in terms of intensity versus channel number.

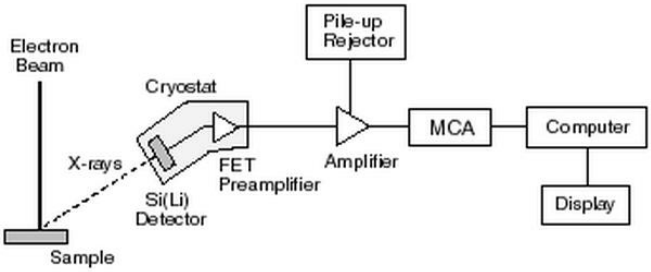

Fig. 2.14 Schematic representation of an energy-dispersive spectrometer [32].

The limitation of EDX is that the elements lighter than sodium (Z=11) cannot be detected. Moreover, Si(Li) detector have to cool in liquid nitrogen temperature, and it is impossible to achieve high sensitivities of weak peaks when strong ones are also presented. It is because all intensity data have to be collected simultaneously and strongest line determines the count rate. The scheme of EDX is shown in Fig. 2.14.

2.4.10 X-ray photoelectron spectroscopy (XPS) [33-34]

After excitation of photon energy ($h\upsilon$) on the surface of material, the ejected photoelectrons have a kinetic energy distribution made up of a series of discrete bands reflecting the electronic structure of the sample. The experimental determination of the kinetic energy (*KE*) of photoelectron enables the binding energy (*BE*) of photoelectron to be calculated from the Eq. 2.20:

$$KE = h\upsilon - BE \quad (2.20)$$

The photoelectron spectrum consists of a series of peaks at discrete values of *KE* corresponding to particular values of *BE*. The KE is modified by the work function of energy analyzer and by several atomic parameters that are associated with the electron emission process. The ejection of one electron leaves behind an excited molecular ion. The electron in the outermost and in other orbitals experiences a change in the effective nuclear charge due to an alteration of screening by other electrons. This may give rise to satellite peaks near the main photoelectron peaks. The other spectral feature is spin-orbit doublet peaks. For example, when a pair of electrons in a 3*p* orbital subshell is photoionized, the remaining electron can have two energetically equivalent final state with spin-up (+1/2) or spin-down (-1/2). Magnetic interaction between the spin of the electron (up or down) and its orbital angular momentum may lead to a splitting of degenerated state into two components. This is called spin-orbit coupling or *j-j* coupling (*j*, quantum number = $l+s$). Therefore, each level with $l \geq 1$, (i.e. *p, d* and *f* orbital) shows spin-orbit pairs ($p_{1/2}$, $p_{3/2}$; $d_{3/2}$, $d_{5/2}$ and $f_{5/2}$, $f_{7/2}$). The ratio of their respective degeneracies, $(2j + 1)$, determines the intensities of the peaks. The energy separation of the doublets is in the order of $p > d > f$. Thus, photoelectron peaks from core levels occur in doublets except for s level ($l = 0$) which give a single peak. The value of *BE* enables the identification of this following features.

[a] The atom involved in the ionization process

[b] The chemical environment of a given atom through small change in *BE* (chemical shift).

Photoemission is usually divided into two classes: ultraviolet photoelectron spectroscopy (UPS) and X-ray photoelectron spectroscopy (XPS). The names derive from the energies of photon used in the particular spectroscopy. UPS studies the

properties of valence electrons that are in the outermost shell of the atom and utilizes photons in the UV region of the electromagnetic spectrum. XPS investigates the properties in the inside shells of atoms and uses photons in the x-ray region, such as Mg Kα (1253.6 eV) and Al Kα (1486.6 eV).

XPS can be used to determine the oxidation state of elements at the surface. The electronic binding energy for inner-shell electrons shifts as a result of changes in the chemical environment. The exact binding energy of an electrons essentially depends upon:

(i) The level from which photoemission is occurring
(ii) The oxidation state of atom
(iii) The chemical environment

The aspects of (ii) and (iii) give rise to shift in the photoemission peak positions in the spectrum called chemical shifts. Atoms of higher positive oxidation state exhibit a higher binding energy due to the extra columbic interaction between the photo-emitted electron and the ion core. The charge redistribution of valence electrons induces changes in the BE of the core electrons, so that information on the valence state of the element is readily obtainable.

2.4.11 Transmission Electron Microscopy (TEM) [34]

The images of TEM technique are a result of the interaction between the electron and sample. As seen in Fig. 2.15, the signal of TEM is the transmitted beam that can penetrate a thin sample through the various lens which finally project the images on the screen. The advantage of TEM is obvious, as it permits direct observation and measurement of the metal particles. Most modern electron microscopes have a resolution of 0.2 to 0.3 nm, so it is even possible to visualize the various crystallographic planes. Also, the distance between the crystallographic planes may be studied. It is also possible to measure particle size distributions by using TEM. Since the sample size is very small (less than micrograms), proper sampling and arriving at a representative sample from the bulk of the material are very important. This may perhaps limit the overall results from TEM. The schematic diagram of TEM is shown in Fig. 2.16.

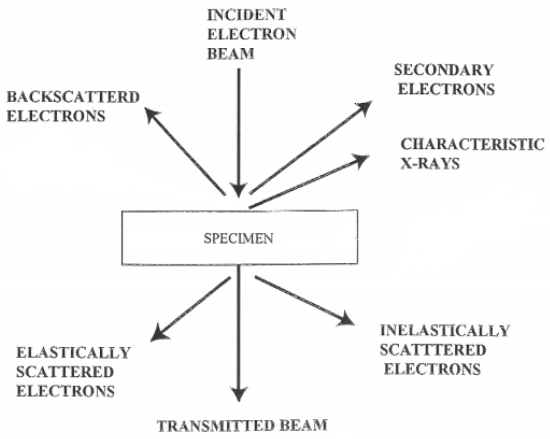

Fig. 2.15 Interaction between electrons and the sample [35].

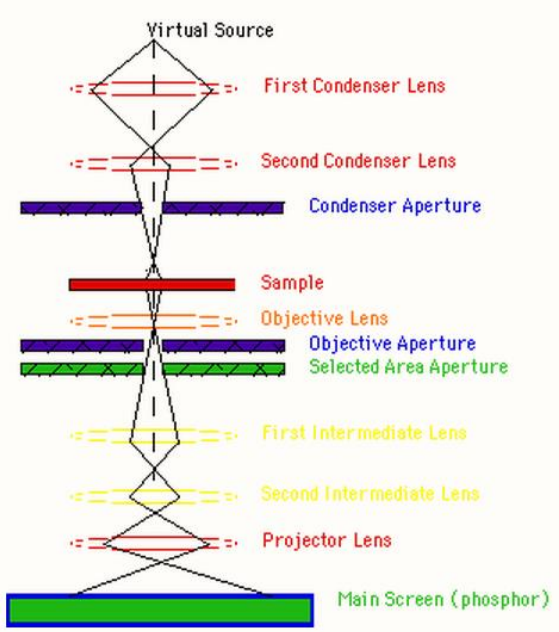

Fig. 2.16 Schematic of light transmission in the TEM instrument [36].

REFERENCES

[1] J. Wormald, P. W. Atkins, J. S. E. Holker, and A. K. Holliday, *In diffraction methods; Oxford Chemistry series*, Clarendon Press: Britain, 1973.

[2] M. Hussain, *Synthesis, Characterization and Applications of Metal Oxide Nanostructures,* LiU-Tryck printed, Sweden 2014.

[3] http://physik2.uni-goettingen.de/research/2_hofs/methods/XRD (12/04/15).

[4] W. Zhou, and Z. L. Wang, *Scanning Microscopy for Nanotechnology*, acid-free paper printed, 2006.

[5] G.-W. Zhou, D. K. Lee, Y. H. Kim, C. W. Kim, and Y. S. Kang. *Bull. Korean Chem. Soc*. **27** (2005) 368.

[6] M. Miler, and M. Gosar, *Geologija*, **52** (2009) 69.

[7] http://www.nanoscience.com/products/sem/technology-overview/how-sem-works/ (12/04/15).

[8] https://www4.nau.edu/microanalysis/Microprobe/Interact-Volume.html (12/04/15).

[9] T. Owen. *In Fundamentals of modern UV-visible spectroscopy*, Agilent Technologies, Germany, 2000.

[10] Q. S. Liu, J. Torrent, V. Barro, Z. Q. Duan, and J. Bloemendal, *Clay Minerals* **46** (2011) 137.

[11] B. Preetha, and C. Janardanan. *Research Journal of Recent Sciences*, **1** (2012) 85.

[12] V. D.-Malic, Z. B.-Mikocevic, and K. Itric, *Technical Gazette* **18** (2011) 117.

[13] A. E. Morales, E. S. A. Mora, and U. Pal, *Revista Mexicana De Fisica S*, **53** (2007) 18.

[14] A. A.A. Ahmed, Z. A. Talib, M. Z. Hussein, M. H. Flaifel, and N. M. A.-Hada, *Journal of Spectroscopy*, **2014 (**2014) 732163.

[15] J. Torrent, and V. Barron, *Clays and Clay Minerals* **51** (2003) 309.

[16] https://www.ssi.shimadzu.com/products/product.cfm?product=uv_accy_ solid guide1 (12/04/15).

[17] T. H. Gfroerer, *In Photoluminescence in Analysis of Surfaces and Interfaces*; R.A. Meyers, John Wiley & Sons Ltd., New Jersey, Canada, 2000.

[18] K. Hannewald, S. Glutsch, and F. Bechstedt, *Physical Review B*, **62** (2000) 4519.

[19] R. C. Evans, P. Douglas, H. D. Burrows, *Applied Photochemistry*, Acid-Free Printed, London, 2013.

[20] http://chemwiki.ucdavis.edu/Physical_Chemistry/Spectroscopy/Electronic_ Spectroscopy/Electronic_Spectroscopy%3A_Theory (12/04/15).

[21] http://cnx.org/contents/7b4dfcf8-b28e-4141-8f2f-1ff39052669f@13.5:30/ Nanomaterials_and_Nanotechnolo (12/04/15).

[22] H. H. Willard, and L. L. Merritt, *JR; John A. Dean; 5th edition*; D. Van Nosyrandcompany, New York, 1974.

[23] B. Stuart, *In Infrared Spectroscopy: Fundamentals and Applications*; A John Wiley & Sons,INC., New Jersey, Canada, 2004.

[24] D. J. Shaw, *Introduction to colloid and surface chemistry; 4th edition*, Butterworth-Heinemann, Birmingham, U.K., 1966.

[25] V. Ponec, Z. Knor, and S. Cerny. *In adsorption on solids*, Butterworth-Heinemann, Birmingham, U.K., 1974.

[26] P. J. V. D. Put, *In the inorganic chemistry of materials*, Plenum press, New York, 1998.

[27] R. T. Yang, *In adsorbents: Fundamentals and applications*, A John Wiley & Sons,INC., New Jersey, Canada, 2003.

[28] S. Brunauer, P. H. Emmett, and E. Teller, *Journal of the American Chemical Society,* **60** (1938) 309.

[29] C. Whiston, *In X-ray methods; Felizabeth Prichard*, A John Wiley & Sons,INC., New Jersey, Canada, 1991.

[30] H. A. V. Sprang, *Advances in X-ray Analysis*, **42** (2000) 1.

[31] http://www.pnsensor.de/Welcome/Research/CCD_for_x-ray/ (12/04/15).

[32] http://www.edu/microanalysis/microprobe/EDS-EDSvsWDS.html (12/04/15).

[33] P. V. D. Heide, *X-ray Photoelectron Spectroscopy; An Introduction to Principles and Practices*, Wiley, Canada, 2012.

[34] B. Viswanathan, S. Sivasanker, A. V. Ramaswamy, *Catalysis Principles and Applications*, Narosa Publishing House, New Delhi Chennai, India, 2006.

[35] http://hrdg.matse.illinois.edu/images/pdf/TEMbasics.pdf (12/04/15).

[36] http://ncmn.unl.edu/cfem/microscopy/TEM.shtml 12/04/15).